

Seasonal variations of the gravity wave momentum flux in the Antarctic mesosphere and lower thermosphere

P. J. Espy and G. O. L. Jones

British Antarctic Survey, Natural Environment Research Council, Cambridge, UK

G. R. Swenson and J. Tang

Department of Electrical and Computer Engineering, University of Illinois at Urbana-Champaign, Urbana, Illinois, USA

M. J. Taylor

Department of Physics, Utah State University, Logan, Utah, USA

Received 12 December 2003; revised 15 April 2004; accepted 21 July 2004; published 8 December 2004.

[1] Airglow imager and dynasonde/imaging Doppler interferometer (IDI) radar wind measurements at Halley Station, Antarctica (75.6°S , 26.6°W) have been used to estimate the seasonal variation of the vertical fluxes of horizontal momentum carried by high-frequency atmospheric gravity waves. The cross-correlation coefficients between the vertical and horizontal wind perturbations were calculated from sodium (Na) airglow imager data collected during the austral winter seasons of 2000 and 2001. These were combined with wind velocity variances from coincident radar measurements to estimate the daily averaged upper limit of the vertical flux of horizontal momentum due to gravity waves. The resulting momentum flux at the Na airglow altitudes, while displaying a large day-to-day variability, showed a marked rotation from the northwest to the southeast throughout the winter season. Calculations show that this rotation is consistent with seasonal changes in the wind field filtering of gravity waves below the Na airglow region. The calculations also indicate that while the magnitude of the meridional wind is small, this filtering leads to the observed seasonal changes in the meridional momentum flux.

INDEX TERMS: 3332 Meteorology and Atmospheric Dynamics: Mesospheric dynamics; 3334 Meteorology and Atmospheric Dynamics: Middle atmosphere dynamics (0341, 0342); 0310 Atmospheric Composition and Structure: Airglow and aurora; 0342 Atmospheric Composition and Structure: Middle atmosphere—energy deposition; **KEYWORDS:** gravity wave, momentum flux, Antarctic, mesosphere

Citation: Espy, P. J., G. O. L. Jones, G. R. Swenson, J. Tang, and M. J. Taylor (2004), Seasonal variations of the gravity wave momentum flux in the Antarctic mesosphere and lower thermosphere, *J. Geophys. Res.*, 109, D23109, doi:10.1029/2003JD004446.

1. Introduction

[2] Although gravity waves have spatial scales of only ten to a few hundred kilometers, and their temporal scales are between five minutes and several hours, they play a major role in the global dynamics, circulation and thermal balance of the mesosphere and lower thermosphere. Typically generated in the lower atmosphere through the action of weather systems or orographic lifting of air masses [Fritts and Alexander, 2003, and references therein], the waves grow in amplitude as they propagate upward into the rarified mesosphere. There, depending upon the filtering action of the winds below, the waves can either accelerate or decelerate the mesospheric wind jets as they become unstable and locally dissipate their energy and momentum [Lindzen, 1981; Holton, 1982, 1983; Garcia and Solomon, 1985; Fritts and Alexander, 2003]. This input of momentum limits the mean zonal mesospheric wind speeds to ~ 70 m/s,

whereas in thermal wind balance with radiative equilibrium they would attain speeds over 300 m/s [Walterscheid, 2001]. This interaction with the mean wind also creates a large departure of mesopause temperatures from radiative equilibrium [Haurwitz, 1961], and results in mean polar summer temperatures as low as 130 K, with winter temperatures approaching 300 K [Garcia and Solomon, 1985; Lübken *et al.*, 1990; Espy and Stegman, 2002].

[3] Given the role of gravity waves in determining global circulation and thermal balance, they are an essential element of global circulation models (GCMs). Although current GCMs explicitly resolve longer-scale gravity waves, shorter-scale waves with periods less than one hour carry the bulk of the energy and momentum to the mesosphere [Vincent, 1984]. Hence much of the gravity wave spectrum that is important for maintaining the mean circulation is not explicitly resolvable in current GCMs, and their effects must therefore be parameterized [Hamilton, 1996]. Most parameterizations require temporal and spatial variations to reproduce the wave-driven circulation effects adequately [e.g., Rind *et al.*, 1988; Hamilton, 1995]. Hence knowledge

of the seasonal and latitudinal behavior of the gravity wave momentum flux is essential to both guide and constrain these parameterizations.

[4] A wide variety of radar techniques have been used to measure the seasonal variation of the gravity wave flux at low-to-high northern latitudes and at low-to-middle southern latitudes [e.g., *Murphy and Vincent*, 1993, and references therein]. In addition, using the optical technique developed by *Gardner et al.* [1999], the seasonal variation of gravity wave momentum flux has been measured at northern midlatitudes [*Swenson et al.*, 1999; *Tang et al.*, 2002]. However, there are few measurements of gravity wave momentum flux in the Antarctic regions where the gravity wave parameterization and its variability are critical for GCM performance [*Garcia and Boville*, 1994; *Hamilton*, 1996].

[5] In this paper, we present optical imaging measurements at high, southern latitudes that provide an independent measure of the cross correlation between the vertical and horizontal wind perturbations caused by gravity waves in the mesosphere. These are combined with radar wind observations to infer an upper limit to the vertical flux of horizontal momentum, and it is found that both the cross-correlation coefficients and the momentum fluxes exhibit a strong seasonal cycle. A calculation of the gravity wave transmission and the saturated wave momentum flux displays the same seasonal variation as the observed flux, reproducing the relative amplitudes for the zonal and meridional components. This study provides an extensive characterization of not only the seasonal variation of the gravity wave momentum flux in the critical Antarctic region, but also the day-to-day variability of that flux.

2. Instrumentation and Observations

[6] The sodium (Na) airglow originates from a thin (~ 8 km thick) layer centered near 90 km. As atmospheric wave disturbances move through this layer, its intensity is modulated because of the wave-induced density and temperature perturbations [*Swenson and Gardner*, 1998]. As part of a collaboration between Utah State University (USU) and the British Antarctic Survey (BAS), observations of the Na night airglow were made using a monochromatic imaging system developed by USU to observe these gravity wave-induced intensity fluctuations in two dimensions. The camera consisted of a cooled (-45°C), bare, 1024-by-1024 charge-coupled device (CCD) array of high quantum efficiency ($\sim 80\%$ at visible wavelengths and $\sim 50\%$ at near infrared wavelengths). In addition, the pixels were binned together in 2-by-2 groups on the CCD chip before readout to improve the signal to noise. This array was coupled to a fast, $f/4$, telecentric lens system that could use narrow bandpass (~ 2 nm) optical filters to produce monochromatic all-sky (180°) images. To isolate the Na emission for these observations, a filter centered at 589 nm with a 2.5 nm band pass was used. Each Na image was integrated on the CCD for 90 s before being digitized to 16 bits. A filter wheel cycled through several other spectral channels, giving the Na filter a repetition rate of ~ 6 min. Since the Na channel was the least susceptible to auroral contamination, it was the only emission used to calculate the momentum flux. With the high sensitivity of camera system, gravity wave

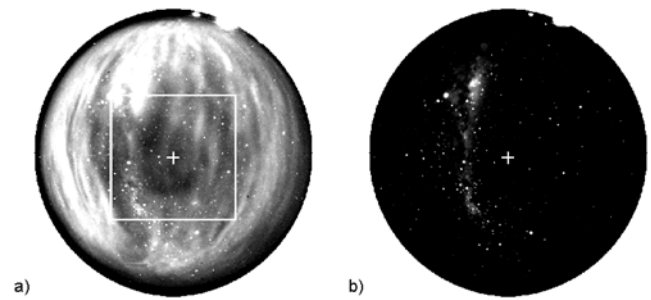


Figure 1. All-sky image (a) in sodium emission and (b) at a background wavelength, shown on the same gray scale range for the night of 20–21 July 2001. North is at the top and east to the right of the images, and the approximate 150-km field of view analyzed is shown on the Na image. Gravity wave structures aligned N-S, and moving toward the west, are apparent in the Na airglow image, while the stellar and galactic backgrounds that must be removed before processing are more obvious in the background image.

perturbations of the Na airglow intensity of a few percent were readily observed. Gravity waves observed in this manner are generally characterized by vertical wavelengths greater than 12 km, short horizontal wavelengths ($\lambda < 150$ km) and large phase speeds ($C_1 > 40$ m/s) [*Swenson and Gardner*, 1998].

[7] Sodium images could be acquired whenever the sun had set 14 or more degrees below the horizon. In addition, the imager could tolerate a partial moon ($\sim 40\%$ disk) at elevations as high as 5 degrees before the CCD saturation spread and contaminated other pixels. Automated software was used so that images were acquired only under these conditions. An example of an all-sky image in the sodium emission for the night of 20–21 July 2001 is shown in Figure 1a. The image clearly shows airglow structure oriented in the north-south direction, and the sequence of images shows this structure to be moving toward the west. Stellar contamination, both in the form of discrete stars and the unresolved galactic component, is also apparent in the image, and was removed as part of the processing [*Tang et al.*, 2003]. This contamination is more evident in the background image shown in Figure 1b, which was taken using a filter centered at 572.5 nm with the same band pass as the Na filter.

[8] The radar at Halley is a digital ionospheric sounder, or dynasonde, upon which the imaging Doppler interferometer (IDI) method has been implemented since 1996 [*Jones et al.*, 1997; *Charles and Jones*, 1999]. The IDI method itself has been described fully [*Adams et al.*, 1985, 1986; *Meek and Manson*, 1987; *Brosnahan and Adams*, 1993], and validated against both incoherent scatter radar winds from 70 to 97 km [*Turek et al.*, 1998] and meteor wind radar winds from 82 to 98 km [*Jones et al.*, 2003]. The processing and radar setup necessary for its implementation on the Halley system have been described in detail in *Jones et al.* [1997]. In brief, the radar operates at 2.75 MHz ($\lambda = 109$ m) with a pulse length of 48 μs and a receiver range sampling of 0.75 km. IDI soundings are made for 102 s, repeating every 5 min, and the echo returns are sorted by height into

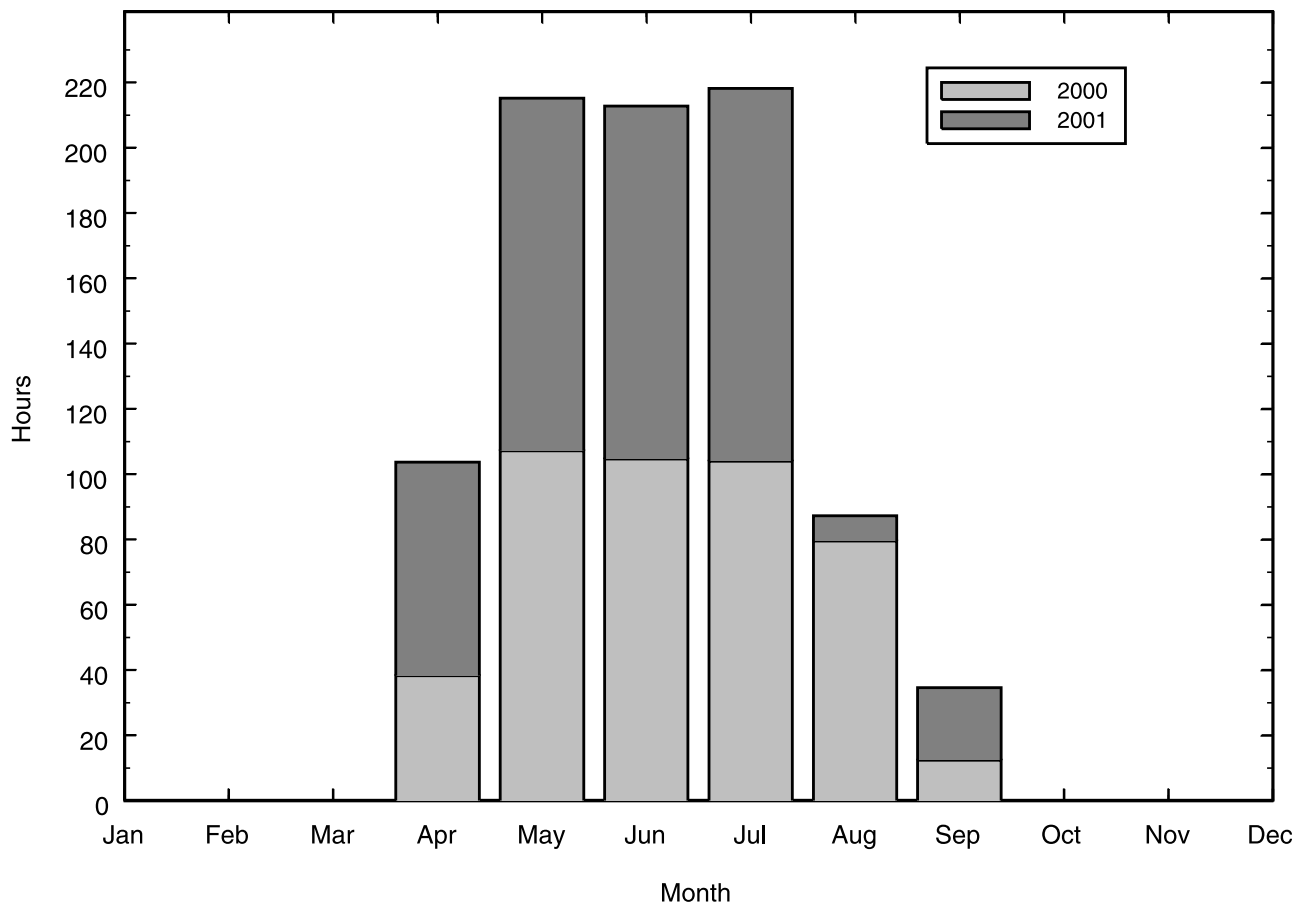


Figure 2. Annual sampling distribution of usable image observations, in hours, for the years 2000 (light gray) and 2001 (dark gray).

5 km bins between 50 and 105 km. The location and line-of-sight velocity of each echo observed in a given height bin are used to fit a single 3-D vector wind for that bin. The resulting time series of wind values are then used to monitor tidal variations and gravity wave fluctuations ($\tau > 10$ min). The precision of the wind estimates are determined by the number of echoes observed, generally lying in the range of ± 4 m/s [Jones *et al.*, 1997] for altitudes above 80 km where most of the IDI echoes are obtained. The radar was run continuously in this mode throughout the observational period with only occasional breaks for maintenance.

[9] The optical and radar observations were carried out at the BAS research station located at Halley, Antarctica over two winter seasons extending from April 2000 through September 2001. Despite the high geographic latitude of Halley, it is situated at lower geomagnetic latitude ($L = 4.5$) than its northern latitude counterparts. However, aurora could occasionally severely contaminate the images. Thus the data for each night were screened for both auroral and meteorological cloud contamination using other broadband spectral channels. For each night, a single contiguous image sequence that was free of aurora and cloud was selected for further analysis. The sequence length varied throughout the season from a maximum near solstice of ~ 19 hours to a minimum of ~ 2 hours near the equinoxes. In total, 40 days in 2000 and 39 days in 2001 were analyzed, and Figure 2 gives the annual sam distribution of usable imager

observations in hours. Wind data collected by the radar was available for all but 4 nights in each of two seasons.

3. Analysis and Results

[10] In this study, the measured azimuthal distribution of the relative airglow intensity variance is used as a proxy for the azimuthal distribution of the horizontal velocity variance in a gravity wave model to predict the momentum flux as a function of azimuth angle. The technique for estimating momentum fluxes using airglow imager data in this way has been described fully by Gardner *et al.* [1999], and can be used to estimate the momentum fluxes associated with the full spectrum of both monochromatic as well as quasi-random wave perturbations. The technique has been validated against Na wind lidar measurements of momentum flux when applied to both monochromatic waves [Swenson *et al.*, 1999] and the full wave spectrum [Gardner *et al.*, 1999], and has been used to infer the seasonal variation of the momentum flux in the northern hemisphere [Tang *et al.*, 2003].

[11] Briefly, the three-dimensional Fourier spectrum in frequency, ω , and the zonal, k , and meridional, l , horizontal wave numbers, was computed for the nightly sequence of all-sky Na images using the processing techniques detailed in Gardner *et al.* [1996] and Coble *et al.* [1998]. The unambiguous two-dimensional horizontal wave spectrum,

which describes the distribution of gravity wave energy as a function of horizontal scale and propagation direction, was computed by integrating the three-dimensional spectrum over frequency. The resulting two-dimensional spectrum included the effects of waves with observed periods between 12 minutes (the temporal Nyquist limit) and 2 hours, and horizontal wavelengths between 2.4 km (the spatial Nyquist limit) and 150 km. Waves with these observed periods are compatible with the spatial sampling of the imager [Gardner *et al.*, 1996], and would not be expected to be Doppler shifted to beyond the Brunt or inertial limits given the low mean wind speeds of between 3 and 9 m sec⁻¹ observed near 90 km at Halley [Charles and Jones, 1999; Fritts and Alexander, 2003]. The unambiguous two-dimensional spectrum was then integrated over the aforementioned horizontal wave number range to create an angular spectrum that shows the distribution of wave energy as a function of propagation direction. This angular spectrum represents the azimuthal distribution of relative Na intensity variance, which may be written as:

$$\frac{\langle I'_{Na}(\phi)^2 \rangle}{\bar{I}_{Na}^2}, \quad (1)$$

where I'_{Na} and \bar{I}_{Na} are the relative perturbation and mean value of the Na emission intensity caused by gravity waves moving in the azimuthal direction, ϕ .

[12] Gardner *et al.* [1999] have shown that this azimuthal distribution of relative Na or hydroxyl airglow intensity variance (equation (1)) is proportional to the azimuthal distribution of the horizontal velocity variance. In turn, the momentum fluxes, or rather the cross-correlation coefficients between the vertical and horizontal winds, can be expressed as a simple integral over the azimuthal distribution of this horizontal velocity variance by using the gravity wave polarization relations and employing a canonical power law model for the frequency distribution of horizontal velocity variance [Gardner *et al.*, 1999]. Thus, by substituting the airglow intensity variance for the horizontal velocity variance, these cross-correlation coefficients between the perturbations of the horizontal and vertical winds may be expressed in terms of the airglow fluctuations [Gardner *et al.*, 1999, equations (26) and (27)] as:

$$\frac{\langle w'u' \rangle}{w'_{rms}u'_{rms}} = \frac{G \cdot \int_0^{2\pi} d\phi \frac{\langle I'_{Na}(\phi)^2 \rangle}{\bar{I}_{Na}^2} \sin(\phi)}{\left[\int_0^{2\pi} d\phi \frac{\langle I'_{Na}(\phi)^2 \rangle}{\bar{I}_{Na}^2} \cdot \int_0^{2\pi} d\phi \frac{\langle I'_{Na}(\phi)^2 \rangle}{\bar{I}_{Na}^2} \sin^2(\phi) \right]^{\frac{1}{2}}} \quad (2)$$

$$\frac{\langle w'v' \rangle}{w'_{rms}v'_{rms}} = \frac{G \cdot \int_0^{2\pi} d\phi \frac{\langle I'_{Na}(\phi)^2 \rangle}{\bar{I}_{Na}^2} \cos(\phi)}{\left[\int_0^{2\pi} d\phi \frac{\langle I'_{Na}(\phi)^2 \rangle}{\bar{I}_{Na}^2} \cdot \int_0^{2\pi} d\phi \frac{\langle I'_{Na}(\phi)^2 \rangle}{\bar{I}_{Na}^2} \cos^2(\phi) \right]^{\frac{1}{2}}}, \quad (3)$$

where w'_{rms} , u'_{rms} and v'_{rms} are the RMS values of vertical and horizontal zonal and meridional wind perturbations. The factor, G , which sets the range of the cross-correlations coefficients, results from the integration over the canonical power law and is a function of the power law spectral index, the Brunt-Väisäällä frequency and the inertial frequency. For the exact form of G and the calculation of uncertainties of the zonal and meridional cross-correlation coefficients, the reader is referred to Gardner *et al.* [1999].

[13] Once the daily cross-correlation coefficients have been determined using the imager data, they may be scaled by the standard deviations of the horizontal and vertical winds determined from the radar to calculate the daily average vertical flux of horizontal momentum. The technique assumes that all the observed waves are propagating upward, that the frequency spectrum follows a canonical power law with spectral slope = 2, and that the velocity spectrum is separable in frequency and azimuth. While these assumptions should not lead to serious errors given the low mean wind environment at Halley [Fritts and Alexander, 2003], the method does not distinguish between propagating and ducted waves, which have no contribution to the vertical flux of horizontal momentum [Fritts, 2000]. This is a shortcoming of the method and hence these results represent an upper limit to the momentum flux. However, Gardner *et al.* [1999] have successfully validated the momentum fluxes derived using this method against those measured directly by a Na wind lidar. Similarly, Tang *et al.* [2002] have used this technique to examine the seasonal variation of gravity wave momentum flux at midlatitudes, finding that ducted waves, typically with wavelengths less than 20 km [Fritts and Alexander, 2003], contributed <10% to the results. Finally, there may be significant uncertainty in the estimation of the radar wind perturbations, particularly in the vertical component. However, while this will lead to a corresponding uncertainty in the actual magnitude of the momentum flux, which is sensitive to the radar wind perturbations, it will be shown that the seasonal variations are determined by changes in the cross-correlation coefficients and not by changes in the RMS wind fluctuations. This is in keeping with the results of Tang *et al.* [2002], who found a similar insensitivity to variations in the RMS wind fluctuations.

[14] To employ this procedure, the true zenith pixel and northward direction were determined using star positions. The images were then recentered on this position and rotated so as to align the cardinal directions along the Cartesian axis. Next, the images were flat fielded to remove van Rijn effect and to correct for the variations in the response of the fish-eye lens and CCD [Coble *et al.*, 1998]. Finally, the stellar contamination was removed using the gradient-based edge technique described by Tang *et al.* [2003]. To avoid the distortions and loss of spatial resolution introduced by the fish-eye lens, only the center 150-by-150 km field of view was interpolated to a 256 square grid on geographic coordinates. The unambiguous two-dimensional Fourier spectrum of the airglow perturbations was then calculated for each night using the sequence of these resampled images [Gardner *et al.*, 1996; Coble *et al.*, 1998; Tang *et al.*, 2002]. The angular spectrum giving the distribution of wave energy as a function of propagation direction was calculated for each night by integrating the resulting

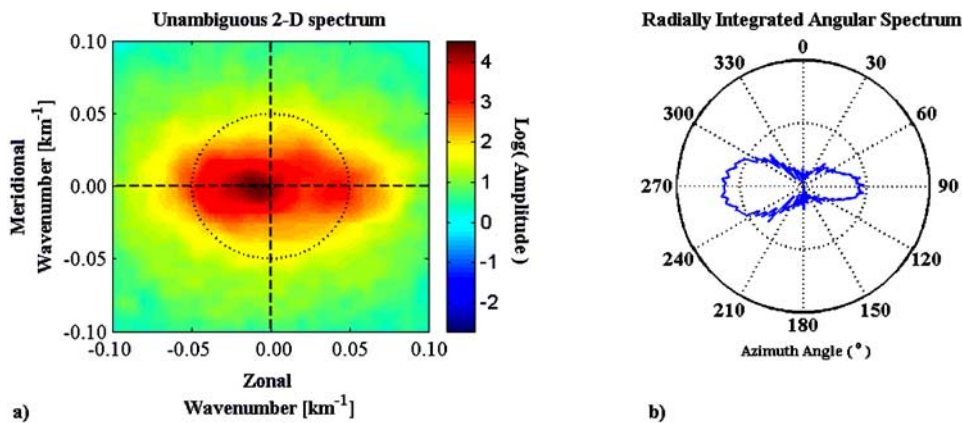


Figure 3. (a) Unambiguous two-dimensional (2-D) horizontal wave number spectrum and (b) angular spectrum for the 10.5-hour sequence of images acquired during the night of 20–21 July 2001. The scales for both spectra are logarithmic, and the 2-D spectrum is in units of (relative percent wave amplitude/wave number)², while the angular spectrum has units of (relative percent wave amplitude)²/rad.

unambiguous Fourier spectrum radially over horizontal wave numbers from $2\pi/(150 \text{ km})$ to $2\pi/(2.4 \text{ km})$, the maximum field and spatial Nyquist limit, respectively. As an example, the unambiguous two-dimensional horizontal wave number spectrum and the angular spectrum for 20–21 July 2001, the same night depicted in Figure 1, are shown in Figure 3. The two-dimensional spectrum in Figure 3a shows that for this night most of the wave energy is located at horizontal wavelengths greater than 12 km and is predominantly in the westward (negative wave number) direction. However, the directionality of the wave field is more clearly indicated by the angular spectrum in Figure 3b, which shows that significantly more energy is propagated westward than eastward. Also apparent is that there are nearly equal amounts of wave energy propagating northward (positive wave number) and southward on this day, which leads to a small net momentum flux meridionally.

[15] Using this angular spectrum, the relative Na intensity variance was then determined as a function of azimuth angle for use as a proxy for the horizontal velocity variance in the expressions for the cross-correlation coefficients between the horizontal and vertical winds [Coble *et al.*, 1998; Gardner *et al.*, 1999]. The IDI radar winds over the Na airglow layer altitude, 90 km, were processed as described above, binned into half-hourly medians, and the mean and tidal components fitted over sliding 4-day intervals removed [Charles and Jones, 1999]. The variance of the residuals was calculated over the same time period as the imager data and used to represent the variance due to gravity waves with periods between 10 minutes (the Nyquist period) and the length of the data segment [Meek *et al.*, 1985]. To estimate the errors associated with these wind variances, this procedure was performed to calculate the daily variance values during 2000 and 2001. During the summer periods, the variance levels were at their lowest, and this value was taken to be the system noise. Although this estimate of uncertainty may contain residual geophysical variations, it represents an upper limit of the uncertainty in the calculated wind variance. These wind variances were then combined with the correlation coefficients so as to determine the nightly averaged vertical flux of horizontal momentum in the zonal and meridional directions, and the error estimates

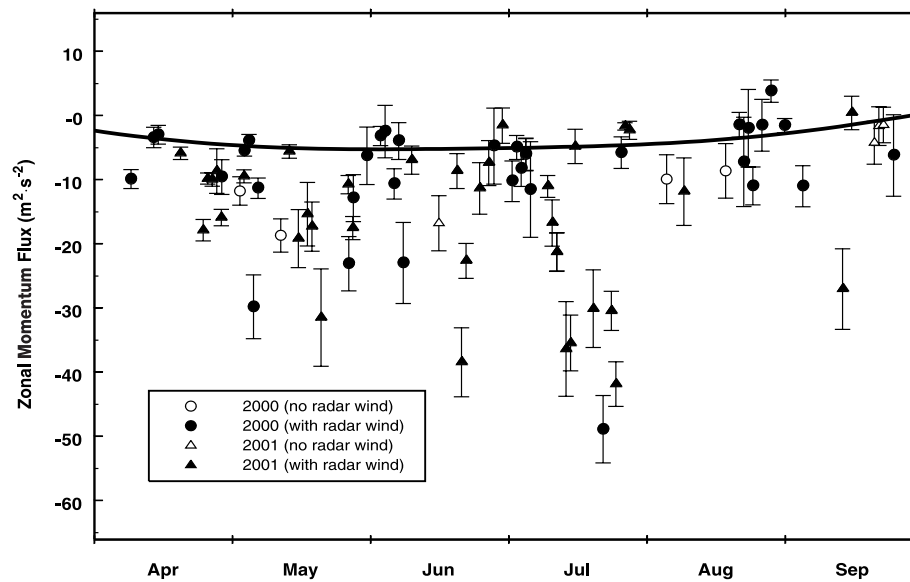
for the variances and correlation coefficients propagated through the calculation to provide an uncertainty estimate for the momentum flux. For the 8 nights where radar winds were not available, the average yearly values of the wind variances were used as scaling factors [Tang *et al.*, 2002].

[16] The results for the two seasons are shown in Figure 4. Here we see that the momentum fluxes in both zonal and meridional directions show a great deal of day-to-day variability, a feature noted in other seasonal studies [Murphy and Vincent, 1993; Swenson *et al.*, 1999; Tang *et al.*, 2002]. However, despite the variability, there is a tendency for the large westward (negative) zonal values to occur near solstice and to decrease to zero near the equinoxes. Those points for which the average values of the wind variances were used as scaling factors, shown by the open data points, do not show a significant trend, indicating that this approximation is justified. Also, the zonal fluxes appear to be generally in the westward direction and much stronger than the northward (positive) tending meridional fluxes. This is shown in the yearly averages, computed using the individual uncertainties as weighting factors, which are listed in Table 1. It is clear that despite the large daily variability, there appears to be little systematic variation between the two years.

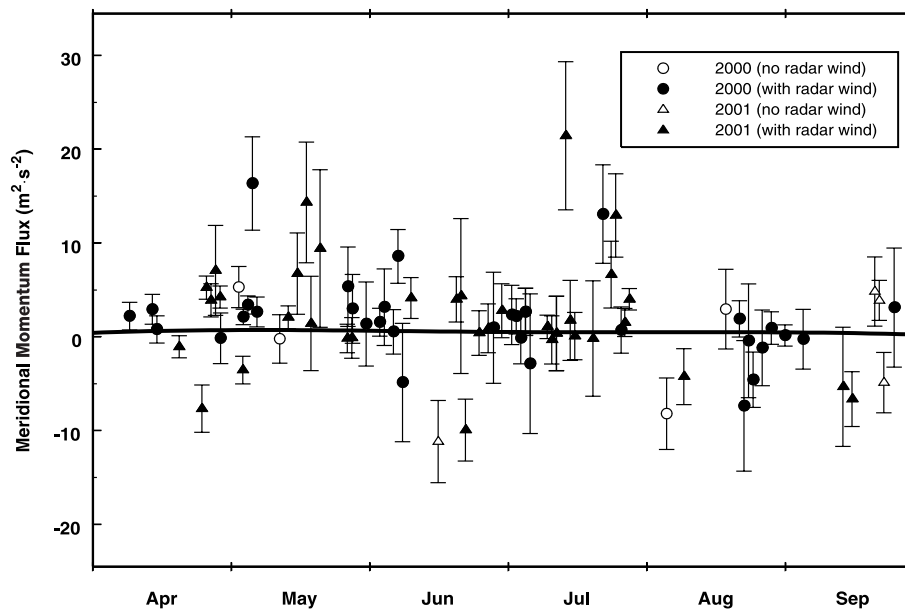
[17] To examine whether the observed seasonal variations are consistent with filtering by the underlying wind field, the gravity wave and momentum flux may be calculated using an appropriate model atmosphere. The gravity wave field observed by the imager will include both freely propagating as well as saturated waves [Gardner and Taylor, 1998]. However, if one takes the saturated waves as a tracer of the wave distribution, then the relative climatological seasonal behavior of the zonal or meridional momentum flux of these gravity waves can be evaluated using the expression given by Holton [1982, 1983]:

$$u'w' = -\frac{\gamma k(\bar{u} - c)^3}{2N}. \quad (4)$$

Here γ , which is less than one, is an “efficiency” factor that accounts for the probability that the waves will not be present at all times [Holton, 1983]. The zonal or meridional



a)



b)

Figure 4. Daily (a) meridional and (b) zonal momentum fluxes for the years 2000 and 2001. The data for 2000 are represented by circles, and those for 2001 are given by triangles. Data for which there are no coincident HF-radar winds are shown by the open symbols. The calculated momentum flux is shown by the solid curve.

wave number of the gravity waves is given by k , which is assumed to be constant for all the waves in the distribution [Holton, 1982, 1983; Garcia and Solomon, 1985], and the zonal or meridional phase speed of these waves is given by c . The scale height, H , the Brunt-Väisälä frequency, N , and the mean zonal or meridional wind, \bar{u} , are evaluated at each altitude for which the flux is to be calculated. This expression was integrated to estimate the relative saturated

Table 1. Yearly Averages of the Momentum Fluxes With Their Standard Errors of the Mean

Year	Zonal Average Plus Eastward Direction, $\text{m}^2 \text{s}^{-2}$	Meridional Average Plus Northward Direction, $\text{m}^2 \text{s}^{-2}$
2000	-4.2 ± 0.8	0.4 ± 0.3
2001	-4.8 ± 0.9	0.8 ± 0.5
Both	-4.4 ± 0.6	0.5 ± 0.2

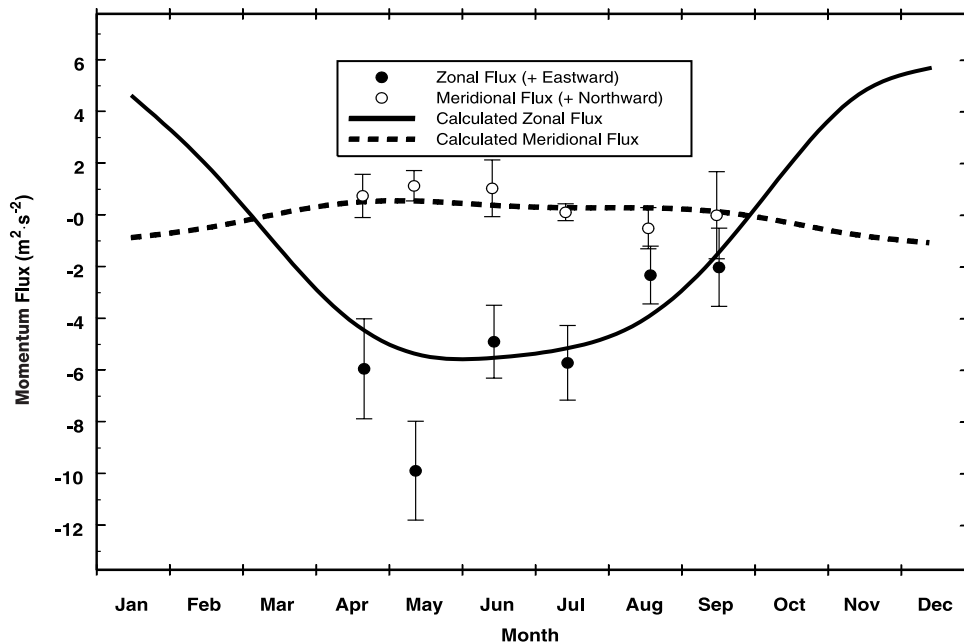


Figure 5. Monthly average zonal (solid circles) and meridional (open circles) momentum fluxes. Also shown are the results of equation (4) calculated using monthly mean values of the HWM-93 wind model for the zonal (solid spline) and meridional (dashed spline) gravity wave momentum flux.

gravity wave momentum flux in the vicinity of the Na emission altitude, ~ 90 km, assuming a phase speed distribution for the initial waves near 10 km that was constant between ± 70 m/s [Alexander and Rosenlof, 1996].

[18] Gravity waves propagating upward from below will not reach heights above which their phase velocity matches the mean wind velocity. To account for this, the Horizontal Neutral Wind Model (HWM-93) [Hedin *et al.*, 1996], run as a monthly mean, was used to eliminate those waves from the distribution reaching 90 km. This procedure did not account for seasonal changes in the gravity wave spectrum, characteristic horizontal scales or the strength of gravity wave sources. However, Alexander [1998] has shown that the background wind filter can reproduce the geographical, seasonal and vertical variations in gravity wave observations without any variations in the spectrum or amplitude of the gravity wave sources in the troposphere. Thus this procedure would appear to be adequate for comparison with the measured momentum flux.

[19] The resulting calculated wave distribution reaching 90 km displayed marked asymmetries due to the filtering of the stratospheric and lower mesospheric winds. This resulted in a strong net flux of westward moving waves at 90 km during the winter, but four times less flux moving eastward during the summer. Similarly, the meridional distribution at 90 km, whose magnitude was ten times less than the zonal component, showed a net flux of northward moving gravity waves during the winter and nearly the same net southward flux during the summer. The relative momentum flux for each month was then calculated by integrating equation (4) over these wave distributions and the HWM-93 winds near 90 km. The resulting zonal and meridional components, scaled by the same horizontal-scale factor, γk , are shown by the solid curves in Figure 4. Despite the variability observations, the calculated

saturated momentum flux reproduces both the westward and northward trends as well as the relative amounts of zonal and meridional momentum flux.

[20] The gravity wave momentum flux measurements from both years were averaged monthly to examine the climatological seasonal behavior. As with the yearly averages, the individual uncertainties were used to weight the values in the average. The resulting monthly averages, along with their standard errors of the mean, are shown in Figure 5. Also shown in Figure 5 are the calculated gravity wave momentum flux values from Figure 4. Both the direction and relative amounts of zonal and meridional momentum flux are in good agreement with the calculated values. In particular, both the imager derived horizontal momentum flux and the calculation show a clear trend to shift from the northwest toward the southeast throughout the winter season, indicating that this behavior is consistent with the filtering of gravity waves by the underlying wind field. This is in agreement with previous southern hemisphere seasonal observations [Murphy and Vincent, 1993], and with a meridional trend opposite that found in the northern hemisphere [Swenson *et al.*, 1999; Tang *et al.*, 2002].

[21] Tang *et al.* [2002] observed very little systematic change in the RMS wind perturbations throughout the year, with the seasonal changes in momentum flux driven by changes in the cross-correlation coefficients. For the present data, Figure 6 shows that there is a strong linear relationship between the monthly averaged momentum fluxes and the corresponding cross-correlation coefficients. Thus a constant, effective RMS wind perturbation product of $43 \pm 5 \text{ m}^2 \text{ s}^{-2}$ for the zonal and $33 \pm 9 \text{ m}^2 \text{ s}^{-2}$ for the meridional direction may be used to scale the cross-correlation coefficients and obtain the momentum flux. These results are consistent with those of Tang *et al.* [2002], who find a

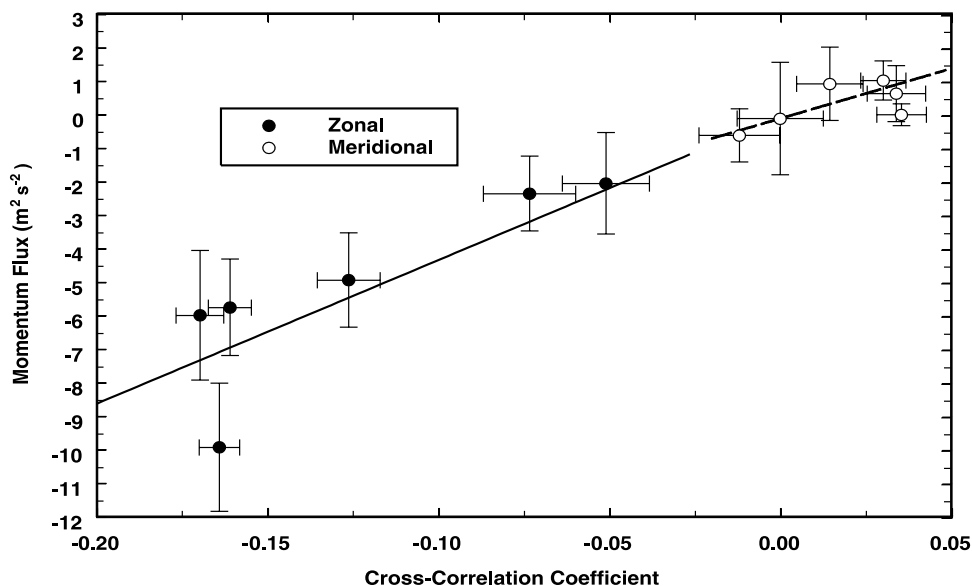


Figure 6. Monthly average zonal (solid circles) and meridional (open circles) momentum fluxes shown as a function of the respective monthly averaged cross-correlation coefficients. A weighted linear regression fitted to the zonal and meridional points is shown by the solid and dashed lines, respectively.

scaling factor of $68 \pm 6 \text{ m}^2 \text{ s}^{-2}$ during the midlatitude winter. Therefore it would appear, in keeping with *Tang et al.* [2002], that the uncertainties in the radar wind perturbations do impact the absolute magnitude of the momentum flux. However, its seasonal variation is determined by changes in the cross-correlation coefficients and not by changes in the RMS wind fluctuations.

4. Discussion and Conclusions

[22] Short-scale gravity waves play an essential role determining the global circulation and thermal balance. GCM parameterizations of these waves must be both guided and constrained by measurements of critical parameters, such as the gravity wave momentum flux and its seasonal variation, particularly in the critical Antarctic regions. To that end, we have used 79 nights, distributed over two years, of Antarctic Na airglow imaging measurements to examine the seasonal variation of the momentum flux of short-scale gravity waves in the mesosphere. The direction and magnitude of the flux were derived using a three-dimensional (two spatial and one temporal) spectral analysis technique on the sequence of images for each night, and combining the results with wind variances from colocated IDI radar measurements.

[23] The results show a great deal of day-to-day variability in the derived momentum flux, but a distinct tendency for the midwinter, strong westward momentum flux to turn eastward near the equinox. Combining the data into monthly averages, a clear seasonal variation showing the turning of the momentum flux from the wintertime northwest direction toward the southeast is seen. Calculations of gravity wave transmission show that the large variation in the thermally driven stratospheric and lower-mesospheric winds creates a similar asymmetry in the direction of the waves reaching 90 km, with even the relatively weak meridional winds giving rise to significant momentum flux. Given the seasonal variability of these meridional winds, it is

not surprising to see the momentum flux directed toward the summer pole [*Tang et al.*, 2002]. A similar scenario occurs in the zonal direction, with the order-of-magnitude larger eastward winds near 90 km leading to a correspondingly larger westward momentum flux during winter.

[24] In conclusion, the observational results presented here show that the horizontal momentum carried upward through the Na airglow region by high-frequency gravity waves in Antarctica is similar in behavior to that observed in the northern hemisphere. That is, wintertime fluxes are predominantly zonal, with individual days showing momentum fluxes of $\sim 50 \text{ m}^2 \text{ s}^{-2}$ in the westward direction. In the meridional direction, the Austral wintertime flux is directed opposite that observed in the Boreal winter, with individual days reaching $20 \text{ m}^2 \text{ s}^{-2}$ in the northward direction (i.e., toward the summer pole) [*Tang et al.*, 2002]. On average, the net wintertime zonal momentum flux is westward with a magnitude of $4.4 \text{ m}^2 \text{ s}^{-2}$, and the meridional average is northward with a magnitude of $0.5 \text{ m}^2 \text{ s}^{-2}$, significantly less than the wintertime magnitudes of $20 \text{ m}^2 \text{ s}^{-2}$ and $12 \text{ m}^2 \text{ s}^{-2}$ in the zonal and meridional directions, respectively, observed at midlatitudes using the same technique [*Tang et al.*, 2002]. As this momentum flux is directed opposite to the mean wind fields, the tendency will be to close off both the zonal and meridional jets in this region, leading to the relatively weak wind velocities observed near 90 km. Thus, while the zonal momentum flux dominates, the flux in the meridional direction cannot be ignored in evaluating the gravity wave forcing of the mesospheric meridional jets that control polar mesospheric temperatures [*Nastrom et al.*, 1982; *Garcia and Solomon*, 1985; *Fritts and Luo*, 1995; *Luo et al.*, 1995].

[25] **Acknowledgments.** The Halley imager was jointly supported by U.S. National Science Foundation grants ATM-0003180 and OPP-9816465, and by the U.K. Natural Environment Research Council. The authors also wish to thank the wintering staff at Halley research station for their efforts.

References

- Adams, G. W., D. P. Edwards, and J. W. Brosnahan (1985), The imaging Doppler interferometer: Data analysis, *Radio Sci.*, *20*, 1481–1492.
- Adams, G. W., J. W. Brosnahan, D. C. Walden, and S. F. Nerney (1986), Mesospheric observations using a 2.66-MHz radar as an imaging Doppler interferometer: Description and first results, *J. Geophys. Res.*, *91*, 1671–1683.
- Alexander, M. J. (1998), Interpretations of observed climatological patterns in stratospheric gravity wave variance, *J. Geophys. Res.*, *103*, 8627–8640.
- Alexander, M. J., and K. H. Rosenlof (1996), Nonstationary gravity wave forcing of the stratospheric mean wind, *J. Geophys. Res.*, *101*, 1571–1588.
- Brosnahan, J. W., and G. W. Adams (1993), The MAPSTAR imaging Doppler interferometer (IDI) radar: Description and first results, *J. Atmos. Terr. Phys.*, *55*, 203–228.
- Charles, K., and G. O. L. Jones (1999), Mesospheric mean winds and tides observed by the imaging Doppler interferometer (IDI) at Halley, Antarctica, *J. Atmos. Sol. Terr. Phys.*, *61*, 351–362.
- Coble, M. R., G. C. Papen, and C. S. Gardner (1998), Computing two-dimensional unambiguous horizontal wavenumber spectra from OH airglow images, *IEEE Trans. Geosci. Remote Sens.*, *36*, 368–382.
- Espy, P. J., and J. Stegman (2002), Trends and variability of mesospheric temperature at high-latitudes, *Phys. Chem. Earth*, *27*, 543–553.
- Fritts, D. C. (2000), Errant influences of gravity wave momentum and heat fluxes using airglow and lidar instrumentation: Corrections and cautions, *J. Geophys. Res.*, *105*, 2355–2360.
- Fritts, D. C., and M. J. Alexander (2003), Gravity wave dynamics and effects in the middle atmosphere, *Rev. Geophys.*, *41*(1), 1003, doi:10.1029/2001RG000106.
- Fritts, D. C., and Z. G. Luo (1995), Dynamical and radiative forcing of the summer mesopause circulation and thermal structure: 1. Mean solstice conditions, *J. Geophys. Res.*, *100*, 3119–3128.
- Garcia, R. R., and B. A. Boville (1994), “Downward control” of the mean meridional circulation and temperature distribution of the polar winter stratosphere, *J. Atmos. Sci.*, *51*, 2238–2245.
- Garcia, R. R., and S. Solomon (1985), The effect of breaking gravity waves on the dynamics and chemical composition of the mesosphere and lower thermosphere, *J. Geophys. Res.*, *90*, 3850–3868.
- Gardner, C. S., and M. J. Taylor (1998), Observational limits for lidar, radar, and airglow imager measurements of gravity wave parameters, *J. Geophys. Res.*, *103*, 6427–6437.
- Gardner, C. S., M. Coble, G. C. Papen, and G. R. Swenson (1996), Observations of the unambiguous 2-dimensional horizontal wave number spectrum of OH intensity perturbations, *Geophys. Res. Lett.*, *23*, 3739–3742.
- Gardner, C. S., K. Gulati, Y. Zhao, and G. Swenson (1999), Measuring gravity wave momentum fluxes with airglow imagers, *J. Geophys. Res.*, *104*, 1903–1915.
- Hamilton, K. (1995), Comprehensive modeling of the middle atmosphere climate: Some recent results, *Clim. Dyn.*, *11*, 223–241.
- Hamilton, K. (1996), Comprehensive meteorological modeling of the middle atmosphere: A tutorial review, *J. Atmos. Terr. Phys.*, *58*, 1591–1627.
- Haurwitz, B. (1961), Frictional effects and the meridional circulation in the mesosphere, *J. Geophys. Res.*, *66*, 2381–2391.
- Hedin, A. E., et al. (1996), Empirical wind model for the upper, middle and lower atmosphere, *J. Atmos. Terr. Phys.*, *58*, 1421–1447.
- Holton, J. R. (1982), The role of gravity wave induced drag and diffusion in the momentum budget of the mesosphere, *J. Atmos. Sci.*, *39*, 791–799.
- Holton, J. R. (1983), The influence of gravity wave breaking on the general circulation of the middle atmosphere, *J. Atmos. Sci.*, *40*, 2497–2507.
- Jones, G. O. L., K. Charles, and M. J. Jarvis (1997), First mesospheric observations using an imaging Doppler interferometer adaptation of the dynasonde at Halley, Antarctica, *Radio Sci.*, *32*, 2109–2122.
- Jones, G. O. L., F. T. Berkey, C. S. Fish, W. K. Hocking, and M. J. Taylor (2003), Validation of imaging Doppler interferometer winds using meteor radar, *Geophys. Res. Lett.*, *30*(14), 1743, doi:10.1029/2003GL017645.
- Lindzen, R. S. (1981), Turbulence and stress owing to gravity-wave and tidal breakdown, *J. Geophys. Res.*, *86*, 9707–9714.
- Lübken, F.-J., et al. (1990), Mean state densities, temperatures and winds during the MAC/SINE and MAC/EPSILON campaigns, *J. Atmos. Terr. Phys.*, *52*, 955–970.
- Luo, Z. G., D. C. Fritts, R. W. Portmann, and G. E. Thomas (1995), Dynamical and radiative forcing of the summer mesopause circulation and thermal structure: 2. Seasonal variations, *J. Geophys. Res.*, *100*, 3129–3137.
- Meek, C. E., and A. H. Manson (1987), Mesospheric motions observed by simultaneous MF interferometer and spaced antenna experiments, *J. Geophys. Res.*, *92*, 5627–5639.
- Meek, C. E., I. M. Reid, and A. H. Manson (1985), Observations of mesospheric wind velocities: 1. Cross section of power spectral density for 48–8 hours, 8–1 hours, and 1 hour to 10 min over 60–110 km for 1981, *Radio Sci.*, *20*, 1383–1402.
- Murphy, D. J., and R. A. Vincent (1993), Estimates of momentum flux in the mesosphere and lower thermosphere over Adelaide, Australia, from March 1985 to February 1986, *J. Geophys. Res.*, *98*, 18,617–18,638.
- Nastrom, G. D., B. B. Balsley, and D. A. Carter (1982), Mean meridional winds in the mid- and high-latitude summer mesosphere, *Geophys. Res. Lett.*, *9*, 139–142.
- Rind, D., R. Suozzo, N. K. Balachandran, A. Lacis, and G. Russell (1988), The GISS global climate-middle atmosphere model: Part I: Model structure and climatology, *J. Atmos. Sci.*, *45*, 329–370.
- Swenson, G. R., and C. S. Gardner (1998), Analytical models for the responses of the mesospheric OH* and Na layers to atmospheric gravity waves, *J. Geophys. Res.*, *103*, 6271–6294.
- Swenson, G. R., R. Haque, W. Yang, and C. S. Gardner (1999), Momentum and energy fluxes of monochromatic gravity waves observed by an OH imager at Starfire Optical Range, New Mexico, *J. Geophys. Res.*, *104*, 6067–6080.
- Tang, J., A. Z. Liu, and G. R. Swenson (2002), High-frequency gravity waves observed in OH airglow at Starfire Optical Range, NM: Seasonal variations in momentum flux, *Geophys. Res. Lett.*, *29*(20), 1966, doi:10.1029/2002GL015794.
- Tang, J., F. Kamalabadi, L. G. Rumsey, and G. R. Swenson (2003), Point source suppression for atmospheric wave extraction from airglow imaging measurements, *IEEE Trans. Geosci. Remote Sens.*, *41*, 146–152.
- Turek, R. S., R. G. Roper, and J. W. Brosnahan (1998), Further direct comparisons of incoherent scatter and medium frequency radar winds from AIDA '89, *J. Atmos. Terr. Phys.*, *60*, 337–347.
- Vincent, R. A. (1984), Gravity-wave motions in the mesosphere, *J. Atmos. Terr. Phys.*, *46*, 119–128.
- Walterscheid, R. L. (2001), Gravity wave transports and their effects on the large-scale circulation of the upper mesosphere and lower thermosphere, *Adv. Space Res.*, *27*, 1713–1721.

P. J. Espy and G. O. L. Jones, British Antarctic Survey, Natural Environment Research Council, High Cross, Madingley Road, Cambridge CB3 0ET, UK. (p.espy@bas.ac.uk)

G. R. Swenson and J. Tang, Department of Electrical and Computer Engineering, University of Illinois at Urbana-Champaign, 313 CSRL, 1308 West Main Street, Urbana, IL 61801, USA.

M. J. Taylor, Department of Physics, Utah State University, Logan, UT 84322, USA.